


 Cite this: *Phys. Chem. Chem. Phys.*,  
 2023, 25, 13429

# Adsorption, activation, and conversion of carbon dioxide on small copper–tin nanoclusters†

 Akshayini Muthuperiyanayagam,<sup>a</sup> Azeem Ghulam Nabi,<sup>abc</sup> Qi Zhao,<sup>id</sup><sup>a</sup>  
 Aman-ur-Rehman<sup>bde</sup> and Devis Di Tommaso<sup>id</sup><sup>\*a</sup>

Carbon dioxide (CO<sub>2</sub>) conversion to value-added chemicals is an attractive solution to reduce globally accelerating CO<sub>2</sub> emissions. Among the non-precious and abundant metals tested so far, copper (Cu) is one of the best electrocatalysts to convert CO<sub>2</sub> into more than thirty different hydrocarbons and alcohols. However, the selectivity for desired products is often too low. We present a computational investigation of the effects of nanostructuring, doping, and support on the activity and selectivity of Cu–Sn catalysts. Density functional theory calculations were conducted to explore the possibility of using small Cu–Sn clusters, Cu<sub>4–n</sub>Sn<sub>n</sub> (*n* = 0–4), isolated or supported on graphene and γ-Al<sub>2</sub>O<sub>3</sub>, to activate CO<sub>2</sub> and convert it to carbon monoxide (CO) and formic acid (HCOOH). First, a detailed analysis of the structure, stability, and electronic properties of Cu<sub>4–n</sub>Sn<sub>n</sub> clusters and their ability to absorb and activate CO<sub>2</sub> was considered. Then, the kinetics of the gas phase CO<sub>2</sub> direct dissociation on Cu<sub>4–n</sub>Sn<sub>n</sub> to generate CO was determined. Finally, the mechanism of electrocatalytic CO<sub>2</sub> reduction to CO and HCOOH on Cu<sub>4–n</sub>Sn<sub>n</sub>, Cu<sub>4–n</sub>Sn<sub>n</sub>/graphene and Cu<sub>4–n</sub>Sn<sub>n</sub>/γ-Al<sub>2</sub>O<sub>3</sub> was computed. The selectivity towards the competitive electrochemical hydrogen evolution reaction on these catalysts was also considered. The Cu<sub>2</sub>Sn<sub>2</sub> cluster suppresses the hydrogen evolution reaction and is highly selective towards CO, if unsupported, or HCOOH if supported on graphene. This study demonstrates that the Cu<sub>2</sub>Sn<sub>2</sub> cluster is a potential candidate for the electrocatalytic conversion of the CO<sub>2</sub> molecule. Moreover, it identifies insightful structure–property relationships in Cu-based nanocatalysts, highlighting the influence of composition and catalyst support on CO<sub>2</sub> activation.

 Received 30th January 2023,  
 Accepted 13th April 2023

DOI: 10.1039/d3cp00477e

[rsc.li/pccp](https://rsc.li/pccp)

## 1. Introduction

The increasing carbon dioxide (CO<sub>2</sub>) level in the environment is the main contributor to global warming.<sup>1</sup> The global temperature has increased by 1 °C compared to the pre-industrial era

and will increase by a further 1.5 °C within the next two decades.<sup>2</sup> One of the solutions is CO<sub>2</sub> utilization, that is, the conversion of captured CO<sub>2</sub> to value-added materials and chemicals.<sup>3</sup> CO<sub>2</sub> conversion is a flourishing area of research as it could use CO<sub>2</sub> as a virtually illimited source of carbon feedstock material. One of the most promising approaches is the electrochemical CO<sub>2</sub> reduction (eCO<sub>2</sub>R) to other C<sub>1</sub> products such as formic acid (HCOOH) and carbon monoxide (CO), and C<sub>2+</sub> substances such as ethylene, ethanol, and others.<sup>2,3</sup> The main challenge in eCO<sub>2</sub>R research lies in the activation of CO<sub>2</sub> minimizing competitive pathways such as the hydrogen evolution reaction (HER, H<sup>+</sup> + e<sup>−</sup> → 1/2H<sub>2</sub>). Thus, catalysts are indispensable for accelerating the eCO<sub>2</sub>R process to recycle CO<sub>2</sub> to value-added chemicals with high faradaic efficiency (FE).

Copper (Cu) is the only metal surface that reduces CO<sub>2</sub> to more than thirty different hydrocarbons and oxygenates.<sup>4</sup> For this reason, Cu is considered the best candidate for eCO<sub>2</sub>R but lacks the required selectivity. For example, the FE achieved for ethylene, the simplest of the C<sub>2</sub> products, is no more than 40% at 200 mA cm<sup>−2</sup>,<sup>5</sup> still too low for practical application.<sup>6</sup> However, the synthesis of small nanoclusters, Cu<sub>*n*</sub> (*n* = 3, 4, 8, 20),

<sup>a</sup> Department of Chemistry, School of Physical and Chemical Sciences,  
 Queen Mary University of London, Mile End Road, London, E1 4NS, UK.  
 E-mail: d.ditomaso@qmul.ac.uk

<sup>b</sup> Department of Physics and Applied Mathematics, Pakistan Institute of Engineering  
 & Applied Sciences, P.O. Nilore, Islamabad, 45650, Pakistan

<sup>c</sup> Department of Physics, University of Gujrat, Jalalpur Jattan Road, Gujrat, Pakistan

<sup>d</sup> Department of Nuclear Engineering, Pakistan Institute of Engineering & Applied  
 Sciences, Nilore, Islamabad 45650, Pakistan

<sup>e</sup> Center for Mathematical Sciences, Pakistan Institute of Engineering & Applied  
 Sciences, Nilore, Islamabad 45650, Pakistan

† Electronic supplementary information (ESI) available: (i) Energies, zero-point energies, and entropies of H<sub>2</sub>(g), CO<sub>2</sub>(g), and CO(g). (ii) Configurations of the initial state, transition state, and final state involved in CO<sub>2</sub> direct dissociation to CO (CO<sub>2</sub>\* → CO\* + O\*) over Cu<sub>4</sub>, Cu<sub>3</sub>Sn, Cu<sub>2</sub>Sn<sub>2</sub>, and CuSn<sub>3</sub>. (iii) Configurations of the intermediates OCHO\*, COOH\*, and \*CO involved in the CO<sub>2</sub> reduction reactions over Cu<sub>4</sub>, Cu<sub>3</sub>Sn, Cu<sub>2</sub>Sn<sub>2</sub>, and CuSn<sub>3</sub>. (iv) CO<sub>2</sub> adsorption, activation and reduction reaction on the isomers of Cu<sub>3</sub>Sn. See DOI: <https://doi.org/10.1039/d3cp00477e>



supported on alumina ( $\text{Al}_2\text{O}_3$ ) exhibited high turnover for the  $\text{CO}_2$  conversion to methanol.<sup>7,8</sup> Larger Cu nanoclusters (1.24 nm) also showed a high FE of 93.5% at  $-0.50$  V (RHE) for  $\text{CO}_2$  reduction to  $\text{CO}$ .<sup>9</sup> A complementary approach to nanostructuring is the incorporation of a second metal<sup>10</sup> to alter the electronic structure (ligand and strain effects)<sup>11</sup> of the host material and the atomic arrangement (geometric ensemble effects) of the active sites. Metal doping can result in the introduction of new active sites in the bimetallic catalyst that are not present in its mono-metallic counterparts. Experimental results also showed that the activity and selectivity of  $\text{eCO}_2\text{R}$  to  $\text{HCOOH}$  and  $\text{CO}$  can be enhanced by incorporating metals such as gold (Au), indium (In), palladium (Pd), cobalt (Co), tungsten (W), and tin (Sn).<sup>12</sup> Au, In and Pd are expensive and/or scarce, whereas Co and W are toxic. Earth-abundant and non-toxic metals such as Sn would be the preferred option for a long-term Cu-based sustainable catalyst solution to  $\text{eCO}_2\text{R}$ . The use of Sn is also attractive because of its high selectivity toward  $\text{C}_1$  products.<sup>13</sup> Cu–Sn catalysts suppress the HER by weakening the binding strength of H and show selectivity for formate ( $\text{HCOO}^-$ ) or  $\text{CO}$  depending on the Cu/Sn ratio.<sup>14</sup> In this regard, a techno-economic evaluation of low-temperature  $\text{CO}_2$  electrolysis showed that achieving high yields of  $\text{C}_1$  products such as  $\text{HCOOH}$  and  $\text{CO}$  is competitive to conventional processes compared to achieving  $\text{C}_2$  products, whose production has substantially higher costs.<sup>15</sup> Consequently, significant progress in the electrochemical  $\text{CO}_2$  reduction to  $\text{C}_1$  products could be achieved using Cu-based alloy clusters doped with earth-abundant metals such as Sn.

The use of small four-atom Cu clusters,  $\text{Cu}_4$ , as catalysts for the conversion of  $\text{CO}_2$ , to not only methanol but also other several chemicals, has been reported in several experimental and theoretical studies.<sup>7,8,16–18</sup> Previous computational work focused on tetrahedral non-supported bimetallic Cu–Pt,<sup>19</sup> Cu–Pd and Cu–Ni,<sup>20</sup> and Cu–Zr.<sup>21</sup> But there is still a lack of understanding regarding the effect of the inclusion of Sn atoms in small copper clusters. Moreover, in the realistic electrocatalytic reaction, a cluster is supported by oxides and other substrates. Lee *et al.* studied  $\text{CO}_2$  conversion on Fe–Cu–K catalysts supported on various oxides, such as  $\text{Al}_2\text{O}_3$ ,  $\text{SiO}_2$ , and  $\text{TiO}_2$ , and found that alumina enhances  $\text{CO}_2$  chemisorption and, therefore, its activation.<sup>9</sup> Another study found stable Cu nanoclusters ( $n = 3, 4, 8, 20$  and so forth) synthesized on alumina ( $\text{Al}_2\text{O}_3$ ) to be active towards  $\text{CO}_2$  conversion to methanol.<sup>7</sup> Similarly,  $\text{Cu}_4$  deposited on  $\text{Al}_2\text{O}_3$  exhibited a high turnover for catalytic  $\text{CO}_2$  hydrogenation.<sup>8</sup> A density functional theory (DFT) study of  $\text{CO}_2$  adsorption on Cu–Co clusters supported on partially hydroxylated  $\text{Al}_2\text{O}_3$  showed that  $\text{CO}_2$  interacts not only with the catalysts but also with the support *via* hydrogen bond with the hydroxyl group or direct bonding of the O atoms of the alumina surface.<sup>22</sup> This process stabilizes and activates the adsorbed  $\text{CO}_2$  species (elongated C–O bonds and reduced O–C–O angle). Apart from metal oxides, graphene, a 2D material, has been used to disperse Cu clusters for the  $\text{eCO}_2\text{R}$  to  $\text{C}_1$  products.<sup>23</sup> Anchoring Cu atoms over defective diamond graphene showed high catalytic activity for the

selective conversion of acetylene to ethylene.<sup>24</sup> Nitrogen-doped (ND) graphene-supported gold clusters catalyse the  $\text{CO}_2$  electroreduction to  $\text{CO}$ .<sup>25</sup> Experimental work showed the efficient formation of two-carbon ( $\text{C}_2$ ) products on small Cu clusters embedded in mesoporous carbon spheres,<sup>26</sup> metal-organic frameworks or Cu-coordinated polymers.<sup>27,28</sup> Li *et al.* studied the catalytic activity of small copper clusters anchored over defective nanodiamond graphene for  $\text{CO}_2$  reduction and found  $\text{Cu}_3/\text{ND}@$ graphene and  $\text{Cu}_4/\text{ND}@$ graphene to convert  $\text{CO}_2$  to  $\text{C}_1$  compounds.<sup>29</sup>

On this basis, we present a systematic computational investigation, based on DFT calculations, of the structure, stability, and electronic properties of the Cu–Sn clusters  $\text{Cu}_{4-n}\text{Sn}_n$  ( $n = 1–4$ ) and compare their results to monometallic  $\text{Cu}_4$  and  $\text{Sn}_4$  systems. We considered a detailed characterization of the adsorption and activation (geometry changes, charge transfer) of  $\text{CO}_2$  on the most stable structure of the monometallic and bimetallic Cu–Sn clusters and their efficacy towards the direct gas-phase dissociation of  $\text{CO}_2$  to  $\text{CO}$  and O fragments. We then compare the free energy profiles for the  $\text{eCO}_2\text{R}$  to  $\text{HCOOH}$  and  $\text{CO}$  on isolated  $\text{Cu}_{4-n}\text{Sn}_n$  ( $n = 1–4$ ) clusters as well as on clusters supported on graphene ( $\text{Cu}_{4-n}\text{Sn}_n/\text{graphene}$ ) and on the partially hydroxylated (110) surface of  $\gamma\text{-Al}_2\text{O}_3$  ( $\text{Cu}_{4-n}\text{Sn}_n/\gamma\text{-Al}_2\text{O}_3$ ). Finally, the free energies of the competitive HER on  $\text{Cu}_{4-n}\text{Sn}_n$ ,  $\text{Cu}_{4-n}\text{Sn}_n/\text{graphene}$  and  $\text{Cu}_{4-n}\text{Sn}_n/\gamma\text{-Al}_2\text{O}_3$  were also computed, from which we could conclude on the effect of composition and support on the selectivity towards  $\text{CO}$  or  $\text{HCOOH}$ .

## 2. Computational details

### 2.1 Computational methods

All DFT calculations were conducted with the “Vienna *ab initio* simulation package” (VASP, version 6.3.0)<sup>30</sup> together with the Perdew–Burke–Ernzerhof (PBE) exchange correlation functional<sup>31</sup> and the dispersion correction (Grimme’s-D3).<sup>32,33</sup> A single ( $1 \times 1 \times 1$ ) *k*-point and a ( $3 \times 3 \times 1$ ) mesh were used for the nanoclusters and surface models, respectively, to sample the Brillouin zone of the simulation supercell. A plane-wave basis set within the framework of the projector augmented wave method<sup>33</sup> was used with a kinetic energy cutoff set to 450 eV. The transition state structures connecting adsorbed  $\text{CO}_2^*$  and  $\text{CO}^* + \text{O}^*$  were determined using the climbing image nudged elastic band (cNEB) as implemented in VASP.<sup>33,34</sup> The  $\text{eCO}_2\text{R}$  to  $\text{HCOOH}$  and  $\text{CO}$  includes two concerted proton–electron transfer (CPET) steps. For example, the CPET steps leading to  $\text{CO}$  formation are (i)  $\text{CO}_2^* + (\text{H}^+ + \text{e}^-) \rightarrow \text{COOH}^*$  and (ii)  $\text{COOH}^* + (\text{H}^+ + \text{e}^-) \rightarrow \text{CO} + \text{H}_2\text{O}$ .<sup>35</sup> The competitive HER to generate  $\text{H}_2$  involves a single CPET step:  $\text{H}^+ + \text{e}^- \rightarrow 1/2 \text{H}_2$ . The reaction free energies of these CPET steps were calculated using the computational hydrogen electrode (CHE) approach:<sup>36</sup>

$$\Delta G = \Delta E_{\text{DFT}} + \Delta E_{\text{ZPE}} - T\Delta S + \Delta G_{\text{pH}} + \Delta G_{\text{U}} \quad (1)$$

The terms in eqn (1) are the reaction energy,  $\Delta E_{\text{DFT}}$ , computed at the DFT-PBE level including the effect of hydration obtained with the VASPsol implicit solvation model;<sup>37,38</sup> the change of



zero point energy ( $\Delta E_{\text{ZPE}}$ ); the entropy change,  $\Delta S$ , and the temperature,  $T$ , of the system set at 298.15 K; the free energy correction due to the difference in proton concentration,  $\Delta G_{\text{pH}} = 2.303 \cdot k_{\text{B}} \cdot T \cdot \text{pH}$  (pH = 0 as assumed in this paper); and the free energy correction due to the difference in electrode potential,  $\Delta G_{\text{U}} = -neU$ , where  $n$  is the number of electrons transferred,  $e$  is the electronic charge, and  $U$  is the applied potential ( $U = 0$  as assumed in this paper). The zero-point energies and entropies were determined within the harmonic approximation by taking the vibrational frequencies of adsorbates and molecules calculated with DFT. Based on previous studies using the CHE model,<sup>39</sup> the variations in  $E_{\text{ZPE}}$  and  $S$  were considered to be small compared to variations in the reaction energies based on  $E_{\text{DFT}}$  alone and, therefore, to be constant for all systems in this study.

## 2.2 Computational models

The structures of Cu–Sn nanocluster models were identified using the *ab initio* random structure searching (AIRSS) code,<sup>40</sup> an unbiased approach that has been used extensively to predict the structure of a variety of materials, including clusters.<sup>41,42</sup> The starting point for each calculation is a set of atoms corresponding to the monometallic, ( $\text{Cu}_4$ ) and ( $\text{Sn}_4$ ), and bimetallic,  $\text{Cu}_{4-n}\text{Sn}_n$  ( $n = 1-3$ ), clusters placed randomly within the central volume of a large cube of edge length 20 Å to minimize the interactions between the periodic images. For each system, we generated fifty random structures. The efficiency of the searches was improved by employing constraints on the minimum interatomic separations of the initial structure:  $d(\text{Cu}-\text{Cu}) = 2.1$  Å and  $d(\text{Sn}-\text{Sn}) = 2.6$  Å.<sup>42</sup> The energies of the atomic structures generated by AIRSS were determined with VASP. From the DFT energies of the random structure, the Boltzmann factor  $f_i$  corresponding to each  $i$ th isomer was evaluated according to the expression

$$f_i = \frac{e^{-(E_i - E_0)/RT}}{\sum_j e^{-(E_j - E_0)/RT}} \quad (2)$$

where  $E_i$  is the energy of the  $i$ th candidate structure and  $E_0$  is the energy of the most stable candidate structure. We selected the candidates with a Boltzmann factor  $f_i \geq 0.01$  and, to increase our sampling, we also considered ten to fifteen randomly selected structures such that  $1 \leq E_i - E_0 \leq 3$  eV. These structures were subject to geometry optimization to determine the most stable Cu, Sn and Cu–Sn clusters. During structural relaxation, we used a convergence criterion of  $10^{-6}$  eV for the energy change and  $0.01$  eV Å<sup>-1</sup> for the forces. The structures of the most stable clusters were supported on graphene and on the (110) surface of  $\gamma\text{-Al}_2\text{O}_3$ . The coordinates of  $\gamma\text{-Al}_2\text{O}_3$  ( $P2_1/m$  space group)<sup>43</sup> were used as the starting geometry to optimize the internal coordinates and cell parameters of the bulk structure of  $\gamma\text{-Al}_2\text{O}_3$ .<sup>44</sup> The values of the optimized lattice parameters of  $\gamma\text{-Al}_2\text{O}_3$  were  $a = 5.538$  Å,  $b = 8.347$  Å,  $c = 8.024$  Å,  $\beta = 90.6^\circ$  and  $\alpha = \gamma = 90.0^\circ$ . Starting from the optimized bulk structure, we generated a  $2 \times 2 \times 1$  supercell of partially hydroxylated slabs of the  $\gamma\text{-Al}_2\text{O}_3$  (110) surface containing three atomic layers. In fact,

previous IR experiments showed that isolated hydroxyl (OH) groups (around  $3701$  cm<sup>-1</sup>) at the  $\gamma\text{-Al}_2\text{O}_3$  surfaces were present even after annealing at  $900$  °C for 30 min.<sup>45</sup> The lattice parameters of the unit cell were  $16.05$  Å and  $10.02$  Å and the vacuum space in the  $z$ -direction was set to  $21.71$  Å. All atoms were relaxed during the optimization. For graphene-supported nanoclusters, a  $5 \times 5 \times 1$  supercell was used. Calculation of the energy of adsorption of the  $\text{Cu}_{4-n}\text{Sn}_n$  ( $n = 0-4$ ) clusters on the graphene and  $\gamma\text{-Al}_2\text{O}_3$  (100) surfaces shows a favorable interaction between the Cu–Sn clusters and the support (Table S2 in the ESI†). The adsorption and dissociation of  $\text{CO}_2$  were studied using the most stable structure of every composition of the  $\text{Cu}_{4-n}\text{Sn}_n$  ( $n = 1-4$ ) clusters. To compute the free energy pathways for the electrochemical conversion of  $\text{CO}_2$  to formic acid ( $\text{CO}_2 + 2\text{H}^+ + 2\text{e}^- \rightarrow \text{HCOOH}$ ) and carbon monoxide ( $\text{CO}_2 + 2\text{H}^+ + 2\text{e}^- \rightarrow \text{CO} + \text{H}_2\text{O}$ ), we started from the most stable optimized structure of adsorbed  $\text{CO}_2^*$  and from it generated and optimised the structure of  $\text{OCHO}^*$ ,  $\text{COOH}^*$  and  $\text{CO}^*$  on the nanoclusters. The structures of all atomistic models generated in this study are provided in Section S2 of the ESI.†

## 3. Results and discussion

### 3.1 Structure, stability, and electronic properties of Cu–Sn clusters

The structures and relative energies of the low energy isomers of the tetrahedral  $\text{Cu}_{4-n}\text{Sn}_n$  ( $n = 0-4$ ) clusters are reported in Fig. 1. Since the thermal energy is  $k_{\text{B}}T = 0.025$  eV at  $T = 298.15$  K, where  $k_{\text{B}}$  is the Boltzmann constant, we expect that for each cluster more than one isomer may coexist at room temperature if their energies are within the 0.25 eV energy range. According to Fig. 1, except for  $\text{Cu}_3\text{Sn}$ , the other bimetallic Cu–Sn clusters and pure  $\text{Cu}_4$  and  $\text{Sn}_4$  exist as one isomer at room temperature because the energy difference between the most stable isomer and its next higher energy isomer is more than 0.25 eV. The ground state of  $\text{Cu}_4$  is a two-dimensional structure with  $D_{2\text{h}}$  symmetry, in agreement with previous studies (Fig. 1a).<sup>7,20,46</sup> The next higher energy isomer of  $\text{Cu}_4$  is also a 2D structure with a planar-triangular geometry and  $C_s$  symmetry, which is 0.4 eV higher in energy than the lowest energy isomer. The bimetallic  $\text{Cu}_3\text{Sn}$  cluster has three isomers with similar energy: the most stable is a distorted three-dimensional (3D) structure with  $C_s$  symmetry, followed by an isomer of tetrahedral geometry (0.06 eV), and an isomer where the planarity of the  $\text{Cu}_4$  cluster is preserved ( $C_{2\text{v}}$  symmetry, 0.17 eV) (Fig. 1b). For  $\text{Cu}_2\text{Sn}_2$ , the distorted 3D ( $C_{2\text{v}}$ ) and tetrahedral ( $D_{2\text{h}}$ ) structures were found to be the most stable isomers but in this bimetallic cluster the energy difference between them is large (0.83 eV) (Fig. 1c). For  $\text{CuSn}_3$ , the ground-state 2D structure with the Sn atoms forms trigonal geometry with the Cu atom at the lateral position, the second most stable isomer is a 3D pyramidal structure, and the least stable one has a 2D rhombus-like geometry (Fig. 1d). Like  $\text{Cu}_4$ , the most stable isomer of the  $\text{Sn}_4$  cluster has a two-dimensional structure with  $D_{2\text{h}}$  symmetry (Fig. 1e). Overall, the four atom clusters of the ground-states of monometallic  $\text{Cu}_4$



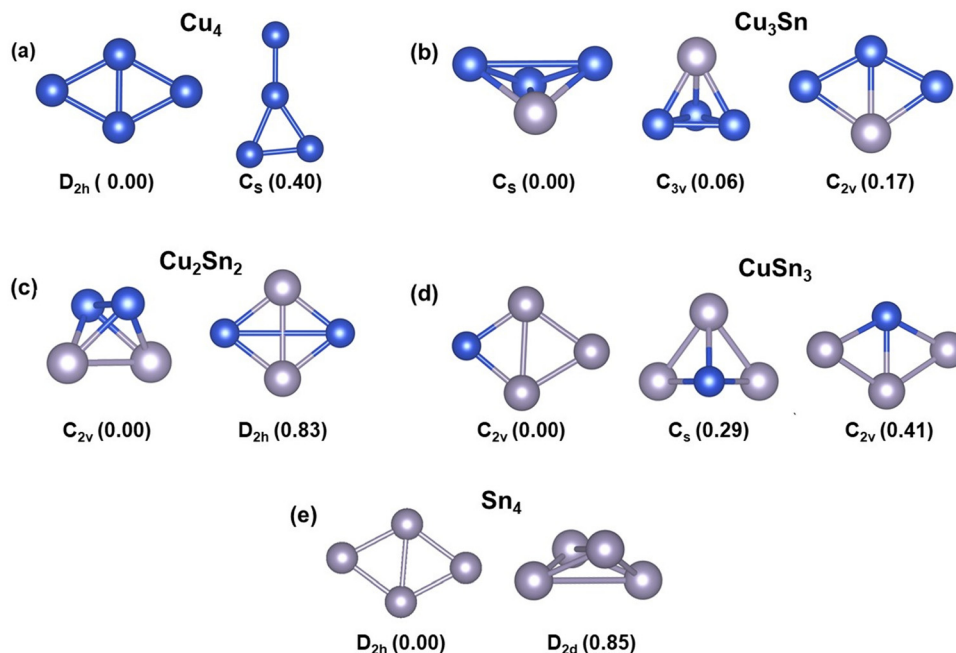


Fig. 1 The lowest energy isomers of the four-atom  $\text{Cu}_{4-n}\text{Sn}_n$  ( $n = 0-4$ ) clusters: (a)  $\text{Cu}_4$ ; (b)  $\text{Cu}_3\text{Sn}$ ; (c)  $\text{Cu}_2\text{Sn}_2$ ; (d)  $\text{CuSn}_3$ ; (e)  $\text{Sn}_4$ . The symmetry of the structures is given at the bottom of each isomer. The values within the parenthesis are the relative energies (in eV) of the cluster relative to the most stable isomer. Blue and grey balls represent Cu and Sn atoms, respectively.

and  $\text{Sn}_4$  have a 2D planar rhombus-like geometry, whereas the mixed Cu–Sn clusters tend to form distorted 3D, tetrahedral, and quasi-planar geometries.

To gain insights into the relative stabilities of pure and bimetallic four-atom systems, we computed the binding energy per atom ( $E_B$ ), here defined as

$$E_B = -\frac{E(\text{Cu}_{4-n}\text{Sn}_n) - (4-n)E(\text{Cu}) - nE(\text{Sn})}{4} \quad (3)$$

where  $E(\text{Cu}_{4-n}\text{Sn}_n)$  is the total energy of the most stable isomer of each  $\text{Cu}_{4-n}\text{Sn}_n$  ( $n = 0-4$ ) cluster, and  $E(\text{Cu})$  and  $E(\text{Sn})$  are the total energies of Cu and Sn atoms, respectively. A higher positive value of  $E_B$  indicates higher thermodynamic stability of the cluster. As the variation of binding energy does not always provide a clear picture of the relative stability of the

nanoclusters, we have also employed the second-order difference in energy ( $\Delta_2E$ ):

$$\Delta_2E(\text{Cu}_n\text{Sn}_m) = E(\text{Cu}_{n+1}\text{Sn}_{m-1}) + E(\text{Cu}_{n-1}\text{Sn}_{m+1}) - 2E(\text{Cu}_n\text{Sn}_m) \quad (4)$$

The  $\Delta_2E$  index assesses the stability of a cluster,  $\text{Cu}_n\text{Sn}_m$ , compared with its neighboring structures,  $\text{Cu}_{n+1}\text{Sn}_{m-1}$  and  $\text{Cu}_{n-1}\text{Sn}_{m+1}$ . A higher value of  $\Delta_2E$  signifies a greater stability for the cluster as compared to its nearest neighbors. Table 1 reports the values of the energy descriptors  $E_B$  and  $\Delta_2E$  together with a list of electronic properties of the clusters: the energy difference between the highest occupied molecular orbital (HOMO) and the lowest unoccupied molecular orbital (LUMO) (HOMO–LUMO gap,  $\Delta_{\text{H-L}}$ ), the Bader charges ( $Q_B$ ) of the Cu and Sn atoms, and the average interatomic distance between nearest neighbors. According to Table 1, the two isomers of  $\text{Cu}_4$

Table 1 Binding energy per atom ( $E_B$ ), second-order energy difference ( $\Delta_2E$ ), HOMO–LUMO gap ( $\Delta_{\text{H-L}}$ ), Bader charge ( $Q_B$ ), and average distance ( $d$ ) between atoms

System	Symmetry	$E_B$ (eV)	$\Delta_2E$ (eV)	$\Delta_{\text{H-L}}$ (eV)	$Q_B(\text{Cu})$ (e)	$Q_B(\text{Sn})$ (e)	$d_{\text{Cu-Cu}}$ (Å)	$d_{\text{Cu-Sn}}$ (Å)	$d_{\text{Sn-Sn}}$ (Å)
$\text{Cu}_4$	$D_{2h}$	1.42	—	0.94	—	—	2.34	—	—
	$C_s$	1.32	—	0.96	—	—	2.32	—	—
$\text{Cu}_3\text{Sn}_1$	$C_s$	1.68	0.08	1.33	−0.67	2.01	2.8	2.53	—
	$C_{3v}$	1.66	—	1.71	−0.64	1.91	2.43	2.53	—
	$C_{2v}$	1.64	—	1.67	−0.61	1.84	2.33	2.54	—
$\text{Cu}_2\text{Sn}_2$	$C_{2v}$	1.92	1.01	0.97	−0.92	0.92	2.49	2.6	2.88
	$D_{2h}$	1.71	—	0.91	−1.68	1.68	3.94	2.52	3.14
$\text{Cu}_1\text{Sn}_3$	$C_s$	1.91	−0.97	1.94	−1.81	0.60	—	2.53	2.84
	$C_s$	1.84	—	1.29	−1.38	0.46	—	2.63	3.04
	$C_{2v}$	1.81	—	1.33	−0.69	0.23	—	2.62	2.78
$\text{Sn}_4$	$D_{2h}$	2.14	—	1.03	—	—	—	—	2.92
	$D_{2d}$	1.93	—	1.62	—	—	—	—	3.27



have the lowest binding energies (1.42 eV for  $D_{2h}$  and 1.32 eV for  $C_s$ ) out of all four-atom clusters. The value of  $E_B$  increases with the incorporation of more Sn atoms, with the maximum value (2.14 eV) computed for the monometallic  $Sn_4$  cluster. Assessing from the binding energies, the stability of the four-atom bimetallic  $Cu_{4-n}Sn_n$  is more than that of pure  $Cu_4$  and it is the highest for  $Cu_2Sn_2$  (1.92 eV). From the results of second-order difference in the energy,  $\Delta_2E$ , we observe that among the three bimetallic Cu–Sn clusters considered here, the lowest energy isomer of  $Cu_2Sn_2$  exhibits greater stability than the respective isomers of  $Cu_3Sn$  and  $CuSn_3$ . In summary, the  $Cu_4$  cluster is thermodynamically the least stable. However, the cluster stability is strongly affected by its composition: the incorporation of Sn stabilizes the Cu–Sn system compared to the pure copper cluster.

From Table 1, the stability correlates with the average interatomic distances in the cluster. The average Cu–Cu distance of the lowest energy isomer is 2.34 Å, in good agreement with other DFT plane wave studies of Cu clusters (2.36 Å).<sup>47</sup> This average interatomic distance increases to 2.92 Å in  $Sn_4$  because of the different atomic radii of Cu (1.28 Å) and Sn (1.41 Å). In the bimetallic clusters, the trend is an increase of Cu–Cu and a decrease of Sn–Sn, while Cu–Sn distances lie between the Cu–Cu and Sn–Sn distances. We also conducted a Bader charge ( $Q_B$ ) analysis to determine the charge distribution in the Cu–Sn clusters.<sup>48–50</sup> In  $Cu_3Sn$ ,  $Cu_2Sn_2$  and  $CuSn_3$ , the copper and tin atoms have negative and positive Bader charges, respectively (see Table 1). Consequently, during the reduction reaction, the electron transfer process will occur from the electron-rich Cu atoms to the C atom of  $CO_2$ , which is in its highest oxidation state. A descriptor to analyze the global reactivity is the gap energy,  $\Delta_{H-L}$ . This property relates to the energy cost for an electron to jump from the HOMO to the LUMO orbital and, therefore, characterizes the chemical stability of the system, with a higher value of  $\Delta_{H-L}$  corresponding to a more chemically stable (less reactive) cluster. If we compare the values of  $\Delta_{H-L}$  of the most stable isomers of each monometallic and bimetallic cluster,  $Cu_4$  has the lowest HOMO–LUMO gap (0.94 eV). This value increases substantially for  $Cu_3Sn$  (1.33 eV) and  $CuSn_3$  (1.94 eV) but is similar in  $Cu_2Sn_2$  (0.97 eV). In summary, from the energy descriptors  $E_B$  and  $\Delta_2E$  and the electronic descriptor  $\Delta_{H-L}$ ,  $Cu_2Sn_2$  is the most stable cluster and maintains the reactivity of the pure copper cluster.

### 3.2 The adsorption and activation of $CO_2$

The activation of  $CO_2$  is a result of the electronic charge transfer from the HOMO of the cluster to the LUMO of the  $CO_2$  molecule.<sup>51</sup> To investigate the direction of charge migration between the clusters and  $CO_2$ , we have compared in Fig. 2 the energies of the HOMO and LUMO of the most stable isomers of Cu–Sn with those of gas-phase  $CO_2$ . For all clusters, the energy difference between the HOMO of  $CO_2$  and the LUMO of the clusters (dark grey dashed line) is higher than the energy difference between the HOMO of the clusters and the LUMO of  $CO_2$  (blue dashed line). For example, the energy difference between the HOMO of  $Cu_4$  and the LUMO of  $CO_2$  is 3.38 eV,

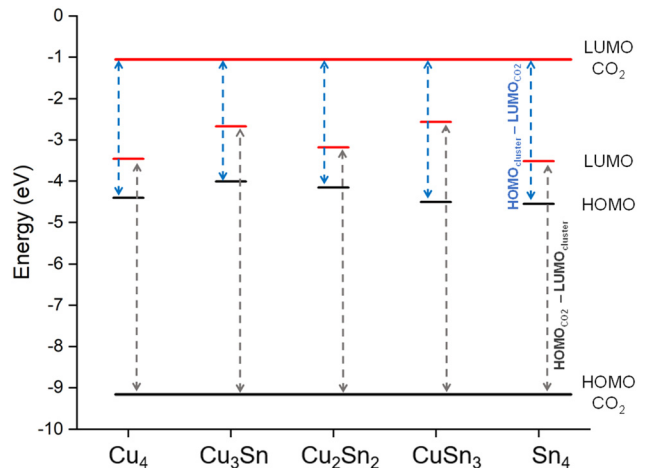


Fig. 2 The HOMO (black line) and LUMO (red line) energy levels of monometallic and bimetallic tetrahedral Cu–Sn clusters compared to that of  $CO_2$ . The dark grey dashed line represents the energy difference between the HOMO of  $CO_2$  and the LUMO of the clusters. The blue dashed line is the energy difference between the HOMO of the clusters and the LUMO of  $CO_2$ .

while the energy difference between the HOMO of  $CO_2$  and the LUMO of  $Cu_4$  is 5.68 eV. Similarly, the energy difference between the HOMO of monometallic  $Sn_4$  and the LUMO of  $CO_2$  is 3.52 eV, while the energy difference between the HOMO of  $CO_2$  and the LUMO of monometallic  $Sn_4$  is 5.62 eV. The charge migration from clusters to the  $CO_2$  molecule is favorable, which results in radical anion  $CO_2^{-\delta}$  formation upon  $CO_2$  adsorption.

The first step in the catalytic conversion of  $CO_2$  is the adsorption process, in which the molecule can physisorb or chemisorb to the catalyst. In the physisorbed state, the  $CO_2$  molecule maintains the C–O bond length (1.18 Å) and the O–C–O bond angle ( $180^\circ$ ) of the gas phase molecule. In contrast, in the chemisorbed state, the  $CO_2$  molecule shows elongated C–O bonds and a decreased O=C=O bond angle (linear to bent mode), which corresponds to the activation of  $CO_2$  because of the charge transferred from the metal catalyst to the  $\pi^*$  molecular orbitals of the  $CO_2$  molecule.<sup>52</sup> Fig. 3 displays the physisorption and chemisorption of  $CO_2$  on monometallic and bimetallic four-atom  $Cu_{4-n}Sn_n$  ( $n = 0-4$ ) clusters. When physisorbed,  $CO_2$  prefers “top” coordination with the O interacting with the Cu atom. When chemisorbed,  $CO_2$  coordinates at the bridge site between the electron-rich Cu and the electron-deficient Sn (Table 1) leading to the formation of Cu–C and Sn–O bonds. From Fig. 3, we also note that on the pure tin cluster,  $Sn_4$ , we could only locate a weakly physisorbed  $CO_2$  state. We have further characterised in Table 2 the interaction and activation of  $CO_2$  on the  $Cu_{4-n}Sn_n$  ( $n = 0-4$ ) clusters relative to the properties of the  $CO_2$  molecule in gas phase using the following energetic, structural, and electronic indicators: adsorption energy ( $\Delta E_{CO_2}$ ); C–O elongation ( $d_{C-O}$ ); O–C–O angle bending ( $\theta_{OCO}$ ); and charge transfer from the cluster to  $CO_2$  ( $\Delta Q$ ). The adsorption energy ( $\Delta E_{CO_2}$ ) was computed according to the following expression:

$$\Delta E_{CO_2} = E[(Cu_{4-n}Sn_n) \cdot CO_2] - E(CO_2) - E(Cu_{4-n}Sn_n) \quad (5)$$



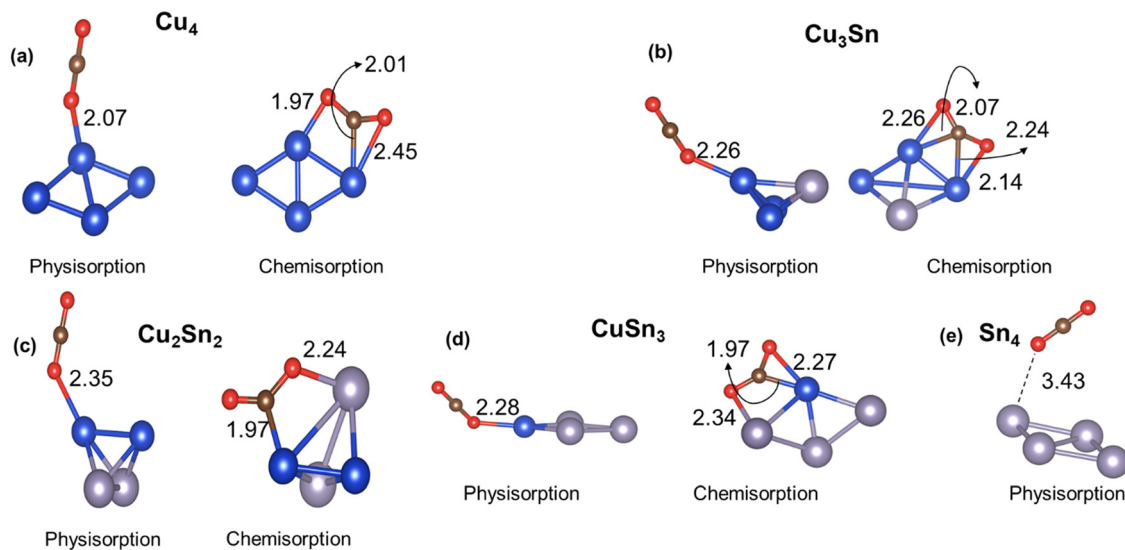


Fig. 3 Lowest energy structures of CO<sub>2</sub> physisorbed and chemisorbed on monometallic and bimetallic Cu–Sn clusters. Blue, grey, brown, and red balls represent Cu, Sn, C and O atoms, respectively.

Table 2 Adsorption energy ( $\Delta E_{\text{CO}_2}$ ), C–O bond length ( $d_{\text{C-O}}$ ), and bond angle ( $\theta_{\text{OCO}}$ ) of CO<sub>2</sub>, and charge transfer from the catalyst to CO<sub>2</sub> using Bader analysis ( $\Delta Q$ ) when physisorbed and chemisorbed on the Cu<sub>4–n</sub>Sn<sub>n</sub> ( $n = 0–4$ ) clusters. For comparison, the bond length and the bond angle of the CO<sub>2</sub> molecule in the gas phase are 1.18 Å and 180 degrees, respectively

System	Physisorption				Chemisorption			
	$\Delta E_{\text{CO}_2}$ (eV)	$d_{\text{C-O}}$ (Å)	$\theta_{\text{OCO}}$ (°)	$\Delta Q$ ( $e$ )	$\Delta E_{\text{CO}_2}$ (eV)	$d_{\text{C-O}}$ (Å)	$\theta_{\text{OCO}}$ (°)	$\Delta Q$ ( $e$ )
Cu <sub>4</sub>	–0.32	1.18, 1.17	179.7	–0.01	–0.53	1.26, 1.22	140	–0.51
Cu <sub>3</sub> Sn	–0.32	1.18, 1.17	179.5	–0.03	–0.21	1.23, 1.24	142.6	–0.52
Cu <sub>2</sub> Sn <sub>2</sub>	–0.14	1.18, 1.17	179.3	–0.02	0.50	1.28, 1.22	132.7	–0.64
CuSn <sub>3</sub>	–0.18	1.19, 1.17	179.6	–0.01	0.40	1.24, 1.27	136.9	–0.70
Sn <sub>4</sub>	–0.16	1.18, 1.80	179.9	0.00	—	—	—	—

where the first term is the energy of the cluster–CO<sub>2</sub> complex, and the second and third terms are the energies of the isolated CO<sub>2</sub> molecule and the pristine cluster, respectively. Here, a negative value of the adsorption energy indicates a favorable interaction between CO<sub>2</sub> and the metal cluster.

The results in Table 2 confirm that when CO<sub>2</sub> chemisorbs to the cluster, there is a significant elongation of the C–O bond, loss of linearity of CO<sub>2</sub>, and charge transfer, which does not occur when CO<sub>2</sub> is physisorbed. For the chemisorbed state, the inclusion of Sn leads to a more pronounced bending of the CO<sub>2</sub> molecule (140.0° for Cu, 142.6° for Cu<sub>3</sub>Sn, 132.7° for Cu<sub>2</sub>Sn<sub>2</sub>, and 136.9° for CuSn<sub>3</sub>) and charge transfer compared to pure Cu (–0.51 $e$  for Cu<sub>4</sub>, –0.52 for Cu<sub>3</sub>Sn, –0.64 $e$  for Cu<sub>2</sub>Sn<sub>2</sub>, and –0.70 $e$  for CuSn<sub>3</sub>). However, there is a counterintuitive behaviour in the inverse relationship between the charge transferred to CO<sub>2</sub> and the adsorption energy: a higher charge transfer from the Cu–Sn cluster to CO<sub>2</sub> does not correspond to a favourable adsorption energy. As shown in Table 2, the interaction of CO<sub>2</sub> on Cu<sub>4</sub> and Cu<sub>3</sub>Sn is favourable for both chemisorption and physisorption ( $\Delta E_{\text{CO}_2} < 0$  in Table 2). On the other hand, for the other Cu–Sn clusters, the CO<sub>2</sub> chemisorption ( $\Delta E_{\text{CO}_2} > 0$ ) is less stable than physisorption ( $\Delta E_{\text{CO}_2} < 0$ ). The higher activation of CO<sub>2</sub> in Sn-bearing clusters (charge transfer

and bending) does not correspond to a favourable interaction between the CO<sub>2</sub> and the catalyst, as previously shown in tetrahedral Cu–Pd, Cu–Ni, and Cu–Zr clusters.<sup>20,21</sup> For the Cu<sub>3</sub>Sn system, we have considered the CO<sub>2</sub> adsorption on the three low-energy isomers in Fig. 1(b) because their energy difference is less than 0.2 eV but, upon optimization, the C<sub>2v</sub> and C<sub>3v</sub> isomers of Cu<sub>3</sub>Sn rearranged to the C<sub>s</sub> isomer (see Fig. S5 in the ESI†). The structures of the Cu<sub>3</sub>Sn⋯CO<sub>2</sub> complex in Fig. 2(b) and the values in Table 2 refer to the lowest energy adsorption site of CO<sub>2</sub>. In comparison, previous DFT calculations of CO<sub>2</sub> adsorption on other four-atom Cu clusters doped with Pd, Ni, Pt and Zr reported values of  $\Delta E_{\text{CO}_2}$  (up to –1 eV) corresponding to more favorable adsorption and Bader charge transfer (up to 1 $e$ ) compared to the Cu–Sn clusters (Table S3 of the ESI†).<sup>18–20</sup> CO<sub>2</sub> is adsorbed weakly on the Cu–Sn clusters compared to Cu–Pd, Cu–Ni, Cu–Pt and Cu–Zr. However, the values of  $\theta_{\text{OCO}}$  and  $d_{\text{CO}}$  are close to those found for Cu–Pd, Cu–Ni, Cu–Pt and Cu–Zr (Table S3, ESI†). Therefore, adsorption energy is not always a good indicator of CO<sub>2</sub> activation.

The adsorption energy, bond length, bond angle, and the overall charge of the CO<sub>2</sub> molecule physisorbed on graphene and  $\gamma$ -Al<sub>2</sub>O<sub>3</sub> supported Cu<sub>4–n</sub>Sn<sub>n</sub> ( $n = 0–4$ ) clusters are reported in Table S4 of the ESI†. For most clusters on graphene and



$\gamma$ -Al<sub>2</sub>O<sub>3</sub>, the physisorption of CO<sub>2</sub> has favourable adsorption energy with a small charge transfer, between  $-0.01e$  and  $-0.03e$ , to the CO<sub>2</sub> molecule. However, for CuSn<sub>3</sub>/graphene and Cu<sub>3</sub>Sn/ $\gamma$ -Al<sub>2</sub>O<sub>3</sub>, CO<sub>2</sub> is in the chemisorbed state, as shown by the significant bending of CO<sub>2</sub> and elongation of C–O (Fig. S3 and S4 of the ESI†). The Bader charge transfer for the chemisorbed CO<sub>2</sub> is between  $-1.0$  and  $-1.6e$ , much higher than that for the unsupported clusters reported in Table 2 ( $-0.5$  to  $-0.7e$ ). However, the chemisorption of CO<sub>2</sub> is not favorable in CuSn<sub>3</sub>/graphene, as evidenced by the positive adsorption energy of 0.34 eV. Similarly, for Cu<sub>3</sub>Sn/ $\gamma$ -Al<sub>2</sub>O<sub>3</sub>, the chemisorption of CO<sub>2</sub> seems to be favorable with a high Bader charge transferred to CO<sub>2</sub>.

### 3.3 CO<sub>2</sub> direct dissociation over Cu<sub>4–n</sub>Sn<sub>n</sub> clusters

The favorable chemisorption on monometallic Cu<sub>4</sub> compared to Cu–Sn clusters motivated us to determine if the activation of CO<sub>2</sub> (chemisorption) affects the kinetic barrier for breaking the C–O bond. To model the gas-phase CO<sub>2</sub> dissociation on the Cu<sub>4–n</sub>Sn<sub>n</sub> ( $n = 0–4$ ) clusters we used the following reaction: CO<sub>2</sub>\* → CO\* + O\*. To this end, we performed transition state search calculations to find the energy barrier to break one of the C–O bonds of the CO<sub>2</sub> molecule. The starting point was the most stable structure of adsorbed CO<sub>2</sub>. The final product was modelled by choosing the most elongated C–O bond of the adsorbed CO<sub>2</sub>, systematically increasing the bond distance to nearly 3.0 Å and optimizing the resulting structure.<sup>21</sup> The relative energies of the reactant complexes (CO<sub>2</sub>\*), transition state (TS) and product complexes (CO\* + O\*) are reported in Fig. 4 together with the structures of these intermediates for Cu<sub>4</sub>. The optimized structures of the initial state, transition state, and final state involved in CO<sub>2</sub> direct dissociation to CO over the other clusters are reported in Fig. S1 of the ESI.† Activation barriers of forward ( $E_{a,f}$ ) and backward ( $E_{a,b}$ ) reactions, the reaction energy ( $\Delta E$ ) measuring the energy difference between the reactant (CO<sub>2</sub>\*) and the product (CO\* + O\*), and

**Table 3** Adsorption energy ( $E_A$ ), forward ( $E_{a,f}$ ) and backward ( $E_{a,b}$ ) activation barriers, reaction energy ( $\Delta E$ ) of the CO<sub>2</sub> direct dissociation (CO<sub>2</sub>\* → CO\* + O\*), and C–O bond distance ( $d_{CO}$ ) of the adsorbed CO fragment in the final dissociated product for CO<sub>2</sub> dissociation over Cu<sub>4–n</sub>Sn<sub>n</sub> ( $n = 0–4$ )

System	$E_A$ (eV)	$E_{a,f}$ (eV)	$E_{a,b}$ (eV)	$\Delta E$ (eV)	$d_{CO}$ (Å)
Cu <sub>4</sub>	−0.53	2.30	2.30	0.00	1.16
Cu <sub>3</sub> Sn <sub>1</sub>	−0.32	2.30	2.09	0.21	1.16
Cu <sub>2</sub> Sn <sub>2</sub>	−0.14	3.14	2.32	0.82	1.15
Cu <sub>1</sub> Sn <sub>3</sub>	−0.18	2.18	2.10	0.08	1.15

the C–O bond distance of the adsorbed CO fragment in the final dissociated product ( $d_{CO}$ ) are summarized in Table 3. The energy barrier to dissociate adsorbed CO<sub>2</sub> and form the CO\* and O\* products is between 2.2 and 3.1 eV. Specifically, the activation energy for the dissociation of CO<sub>2</sub> on Cu<sub>4</sub> is 2.3 eV, which is close to the value of 2.4 eV obtained by Mondal and co-workers using the B3LYP functional with the Stuttgart pseudo-potential basis set (SDD) for Cu and the triple-zeta basis set for C and O.<sup>21</sup> However, another DFT study using the PBE0 functional with the SDD basis set for all atoms gave a much lower barrier of 1.8 eV.<sup>20</sup> The double zeta basis set in these calculations could cause such discrepancy, not observed in our case because of the use in this study of delocalized plane waves to describe all atoms. As the reaction energy over Cu<sub>4</sub> is close to zero, the direct gas-phase CO<sub>2</sub> dissociation could thermodynamically occur on this cluster, but the process is kinetically limited. The results in Table 3 also suggest that except for Cu<sub>2</sub>Sn<sub>2</sub>, the energetics of the CO<sub>2</sub> direct dissociation reaction are not significantly affected by the incorporation of Sn. The activation barrier for Cu<sub>3</sub>Sn is similar to that of monometallic Cu<sub>4</sub> (see Fig. 4). It is the highest for Cu<sub>2</sub>Sn<sub>2</sub> (3.1 eV), and the lowest for CuSn<sub>3</sub> (2.18 eV). The formation of Cu–Sn bonds does not lower the activation energy compared to the monometallic clusters, leading to values for the kinetic barriers close to that found for Cu<sub>4</sub>, suggesting a lack of synergy between copper and tin atoms to modulate activation barriers of the gas-phase CO<sub>2</sub> direct dissociation. In comparison, other reports of four-atom copper-based clusters showed modulation of the activation barriers (higher or lower values of  $\Delta E$  and  $E_{a,f}$ ) depending on the cluster composition. For Cu–Zr, the activation barrier was found to be between 0.13 and 0.52 eV, with Cu<sub>3</sub>Zr having the lowest activation energy but also strong adsorption ( $-3.1$  eV) of the final product (\*CO and O\*), which could lead to poisoning of the catalyst surface.<sup>21</sup> The CO<sub>2</sub> direct dissociation on Cu–Pd clusters had an activation barrier of 1.1 to 2.8 eV, values which are generally lower than those for Cu–Sn (Table 3). The activation barriers of the direct CO<sub>2</sub> dissociation on the Cu–Sn clusters are also higher than those reported for four-atom Pt–Ni clusters.<sup>53</sup>

The adsorption energy of CO<sub>2</sub> on these clusters is significantly lower than the dissociation barrier for the cleavage of the C–O bond, suggesting that the adsorption of CO<sub>2</sub> will be more favorable than the direct dissociation of CO<sub>2</sub>. The positive values of the reaction energy  $\Delta E$ , which is the energy difference between the reaction and the final products, suggest that for Cu<sub>2</sub>Sn<sub>2</sub> and Cu<sub>3</sub>Sn, the dissociation of CO<sub>2</sub> to CO + O is

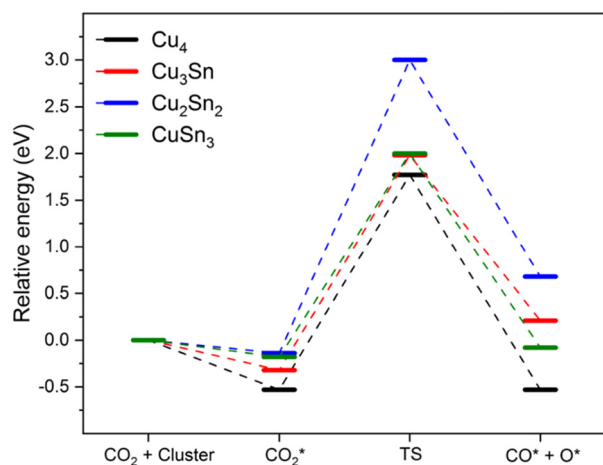


**Fig. 4** Reaction pathway for CO<sub>2</sub> dissociation into CO\* and O\* over Cu<sub>4</sub>, Cu<sub>3</sub>Sn, Cu<sub>2</sub>Sn<sub>2</sub>, and CuSn<sub>3</sub> clusters. The structures are those of the chemisorbed CO<sub>2</sub>, transition state, and (CO\* + O\*) on Cu<sub>4</sub>. Blue, brown, and red balls represent metal Cu, C and O atoms, respectively.



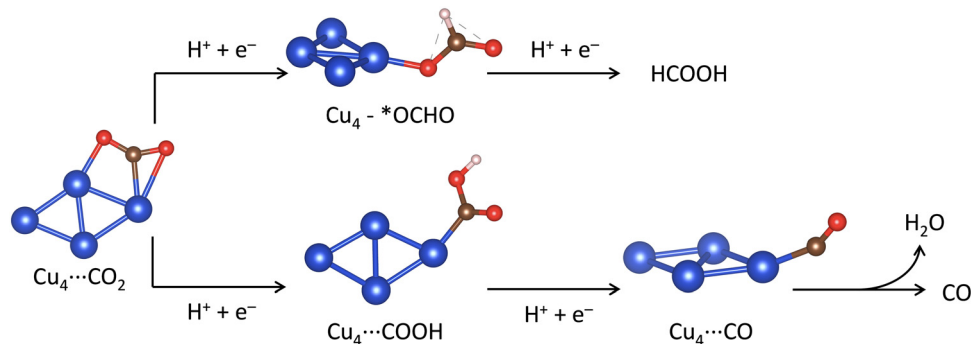


Fig. 5 Reaction pathways for the two proton/two electron ( $2\text{H}^+/2\text{e}^-$ )  $\text{CO}_2$  reduction reaction to carbon monoxide (CO) and formic acid (HCOOH) showing the optimised structures of the intermediates on  $\text{Cu}_4$ . Blue, brown, red and white balls represent metal Cu, C, O and H atoms, respectively.

endothermic. The highly positive  $\Delta E$  of 0.82 for  $\text{Cu}_2\text{Sn}_2$  compared to other clusters indicates that this would have an unstable final product. In summary, the gas-phase  $\text{CO}_2$  direct dissociation,  $\text{CO}_2^* \rightarrow \text{CO}^* + \text{O}^*$ , is kinetically and thermodynamically unfavourable on Cu–Sn clusters and unlikely to occur.

### 3.4 Mechanisms of reduction reactions on Cu–Sn clusters

**3.4.1 Electrochemical  $\text{CO}_2$  reduction to carbon monoxide and formic acid.** In this section, we present calculations of the mechanism of the electrochemical  $\text{CO}_2$  reduction ( $\text{eCO}_2\text{R}$ ) to CO and HCOOH catalyzed by the  $\text{Cu}_{4-n}\text{Sn}_n$  clusters. We have also considered the effects of two supports, graphene and partially hydroxylated  $\gamma\text{-Al}_2\text{O}_3$  (110) surface. The concerted proton–electron transfer (CPET) steps controlling the  $\text{eCO}_2\text{R}$  to HCOOH and CO are shown in Fig. 5. After the adsorption of  $\text{CO}_2^*$  to the catalyst surface, the first CPET step leads to two possible intermediates,  $\text{OCHO}^*$  or  $\text{COOH}^*$ , depending on the atom coordinated to the catalyst: O or C. The second CPET will then form HCOOH or CO accordingly. We have computed the free energy of reactions ( $\Delta G$ ) of the elementary steps leading to the formation of HCOOH and CO. For HCOOH, these steps are the CPET to convert adsorbed  $\text{CO}_2^*$  to an O-coordinated intermediate ( $\text{CO}_2^* + \text{H}^+ + \text{e}^- \rightarrow \text{OCHO}^*$ ,  $\Delta G_{\text{OCHO}^*}$ ) and the next CPET converts adsorbed  $\text{OCHO}^*$  to gas phase formic acid ( $\text{OCHO}^* + \text{H}^+ + \text{e}^- \rightarrow \text{HCOOH}$ ,  $\Delta G_{\text{HCOOH}}$ ). For CO, the elementary steps are the CPET to convert adsorbed  $\text{CO}_2^*$  to a C-coordinated intermediate ( $\text{CO}_2^* + \text{H}^+ + \text{e}^- \rightarrow \text{COOH}^*$ ,  $\Delta G_{\text{COOH}^*}$ ), and the next CPET converts adsorbed  $\text{COOH}^*$  to adsorbed carbon monoxide ( $\text{COOH}^* + \text{H}^+ + \text{e}^- \rightarrow \text{CO}^* + \text{H}_2\text{O}$ ,  $\Delta G_{\text{CO}^*}$ ), which can then be released from the catalyst surface to form gas-phase CO ( $\Delta G_{\text{CO}}$ ).

The Gibbs free energy diagrams of the  $\text{eCO}_2\text{R}$  reaction on the  $\text{Cu}_{4-n}\text{Sn}_n$  ( $n = 0\text{--}4$ ) clusters in Fig. 6(a–d) show that the CPET steps controlling the distribution of the HCOOH and CO products are significantly affected by the cluster composition and the type of support. Graphene-supported Cu–Sn clusters give lower energetic pathways for CO and HCOOH compared to  $\gamma\text{-Al}_2\text{O}_3$ . The optimized structures of the intermediates involved in the  $\text{eCO}_2\text{R}$  on the isolated and supported  $\text{Cu}_4$  clusters are shown in Fig. 7. The Gibbs free energy diagram for the  $\text{eCO}_2\text{R}$

pathways to HCOOH and CO on each Cu–Sn cluster is discussed in detail below. The optimized structures of the intermediates  $\text{CO}_2^*$ ,  $\text{OCHO}^*$ ,  $\text{COOH}^*$ , and  $\text{CO}^*$  adsorbed on  $\text{Cu}_4$ ,  $\text{Cu}_4/\text{graphene}$ , and  $\text{Cu}_4/\gamma\text{-Al}_2\text{O}_3$  are shown in Fig. 7. The intermediates over the other Cu–Sn clusters are reported in Fig. S2 and S4 of the ESI.†

**$\text{Cu}_4$ .** According to Fig. 6(a), the adsorption of  $\text{CO}_2$  is favorable on  $\text{Cu}_4$  and  $\text{Cu}_4/\text{graphene}$  but not on  $\text{Cu}_4/\gamma\text{-Al}_2\text{O}_3$  ( $\Delta G_{\text{CO}_2^*} = 0.6$  eV). On  $\text{Cu}_4$ , the  $\text{eCO}_2\text{R}$  is selective towards HCOOH because of the lower free energy of the  $\text{OCHO}^*$  intermediate ( $\Delta G_{\text{OCHO}^*} = 0.7$  eV) compared to  $\text{COOH}^*$  ( $\Delta G_{\text{COOH}^*} = 1.0$  eV). On  $\text{Cu}_4/\gamma\text{-Al}_2\text{O}_3$ , the intermediate  $\text{OCHO}^*$  binds strongly to the catalyst ( $\Delta G_{\text{OCHO}^*} = -1.8$  eV) compared to  $\text{COOH}^*$  ( $\Delta G_{\text{COOH}^*} = -0.9$  eV). Consequently, the subsequent CPET step favors CO formation as it is easier to release CO as a product from the catalyst than HCOOH. For  $\text{Cu}_4/\text{graphene}$ , the selectivity is towards CO formation as it is easier to form  $\text{COOH}^*$  ( $\Delta G_{\text{COOH}^*} = -0.4$  eV) than  $\text{OCHO}^*$  ( $\Delta G_{\text{OCHO}^*} = 0.5$  eV). In addition, the next CPET step from  $\text{COOH}^*$  to  $\text{CO}^*$  is also favorable ( $\Delta G_{\text{CO}^*} = -0.2$  eV). In summary, while the isolated  $\text{Cu}_4$  is selective towards HCOOH, the effect of both graphene and  $\gamma\text{-Al}_2\text{O}_3$  (110) is to drive the reaction towards CO formation. However, the strong binding of  $\text{OCHO}^*$  on  $\text{Cu}_4/\gamma\text{-Al}_2\text{O}_3$  could poison the  $\text{eCO}_2\text{R}$  on this catalyst.

**$\text{Cu}_3\text{Sn}$ .** In Fig. 6(b), the CPET steps leading to the formation of  $\text{OCHO}^*$  ( $\Delta G_{\text{OCHO}^*} = -0.9$  eV) and  $\text{COOH}^*$  ( $\Delta G_{\text{COOH}^*} = -0.9$  eV) on the most stable isomer of  $\text{Cu}_3\text{Sn}$  ( $C_s$ ) are both exergonic and the subsequent steps to generate HCOOH ( $\Delta G_{\text{HCOOH}} = 1.4$  eV) and CO ( $\Delta G_{\text{CO}^*} = 1.1$  eV) are highly endothermic. The Gibbs free energy diagrams for the other two isomers of  $\text{Cu}_3\text{Sn}$  are given in Fig. S6 (ESI†). On  $\text{Cu}_3\text{Sn}/\gamma\text{-Al}_2\text{O}_3$ , the strong binding of the  $\text{OCHO}^*$  intermediate makes the formation of HCOOH ( $\Delta G_{\text{HCOOH}} = 1.9$  eV) highly unfavourable compared to  $\text{CO}^*$  ( $\Delta G_{\text{CO}^*} = 0.8$  eV). The subsequent step to release CO is exergonic ( $\Delta G_{\text{CO(g)}} = -0.5$  eV). Unlike  $\text{Cu}_3\text{Sn}$  and  $\text{Cu}_3\text{Sn}/\gamma\text{-Al}_2\text{O}_3$ , on graphene the energetics for the reaction steps leading to HCOOH and CO are similar. The formation of  $\text{OCHO}^*$  ( $\Delta G_{\text{OCHO}^*} = 0.2$  eV) is slightly favored compared to  $\text{COOH}^*$  ( $\Delta G_{\text{COOH}^*} = 0.3$  eV). However, the next step from





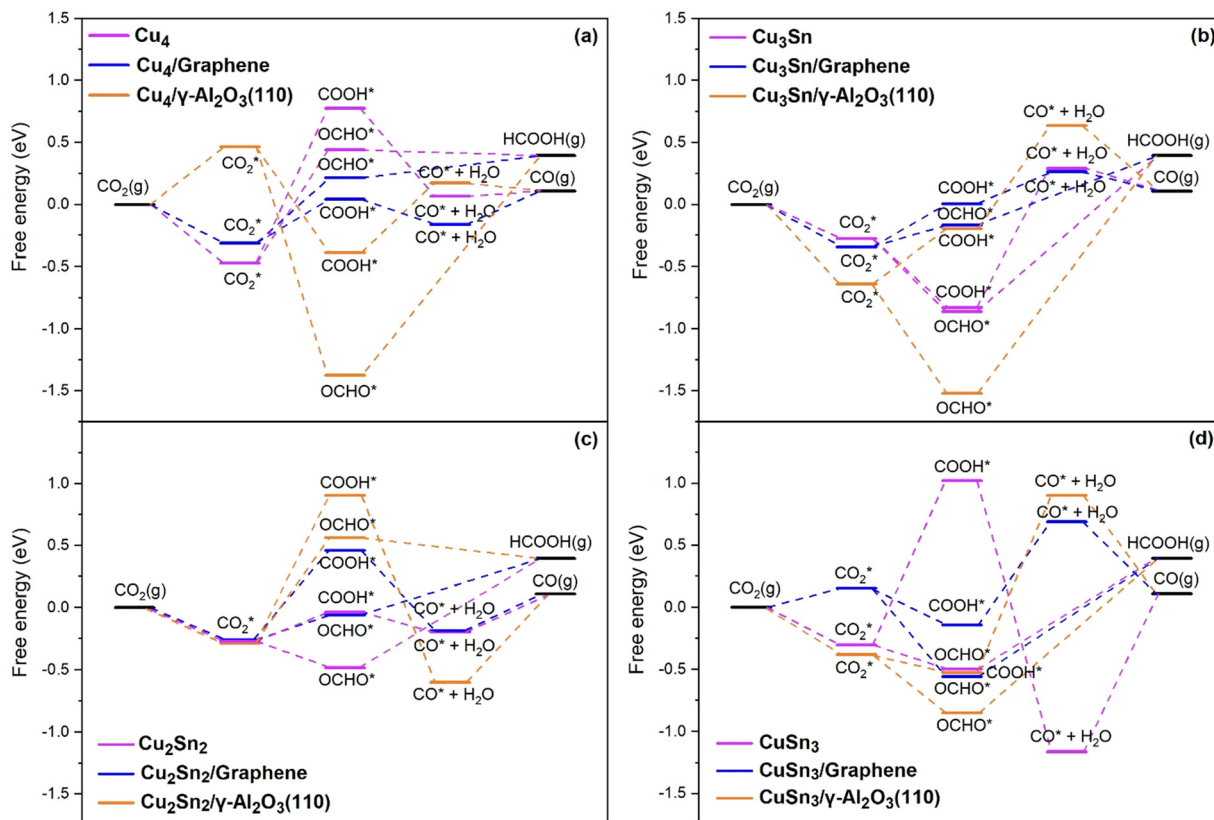


Fig. 6 Gibbs free energy diagram for the eCO<sub>2</sub>R pathways to HCOOH and CO on the (a) Cu<sub>4</sub>, (b) Cu<sub>3</sub>Sn, (c) Cu<sub>2</sub>Sn<sub>2</sub>, and (d) CuSn<sub>3</sub> clusters. Reduction pathways on isolated Cu<sub>4–n</sub>Sn<sub>n</sub> (*n* = 1–3) clusters (light purple) and clusters supported on graphene (blue) and on the partially hydroxylated (110) surface of  $\gamma$ -Al<sub>2</sub>O<sub>3</sub> (orange).

\*OCHO to HCOOH(g) has higher positive free energy ( $\Delta G_{\text{HCOOH(g)}} = 0.6$  eV) relative to the formation of CO\* ( $\Delta G_{\text{CO}^*} = 0.3$  eV), whose desorption energy from the surface ( $\Delta G_{\text{CO(g)}}$ ) is  $-0.2$  eV.

**Cu<sub>2</sub>Sn<sub>2</sub>.** For the Cu<sub>2</sub>Sn<sub>2</sub> system, the \*OCHO intermediate ( $\Delta G_{\text{OCHO}^*} = -0.2$  eV) is more stable than \*COOH ( $\Delta G_{\text{COOH}^*} = 0.3$  eV), but, overall, the energy pathway of CO formation ( $\Delta G_{\text{CO}^*} = -0.2$  eV) is lower than that of HCOOH(g) formation ( $\Delta G_{\text{HCOOH(g)}} = 0.8$  eV). This Cu–Sn cluster is, therefore, selective towards CO. The support effect is destabilizing both \*OCHO and \*COOH intermediates. On Cu<sub>2</sub>Sn<sub>2</sub>/graphene, the \*OCHO formation ( $\Delta G_{\text{OCHO}^*} = 0.2$  eV) is more favorable than \*COOH formation ( $\Delta G_{\text{COOH}^*} = 0.7$  eV) and the overall selectivity is towards HCOOH compared to CO as it has the lowest energetic pathway. On the Cu<sub>2</sub>Sn<sub>2</sub>/ $\gamma$ -Al<sub>2</sub>O<sub>3</sub> system, the first CPET steps to form COOH\* ( $\Delta G_{\text{COOH}^*} = 1.2$  eV) and OCHO\* ( $\Delta G_{\text{OCHO}^*} = 0.8$  eV) are both highly unfavorable. The overall product selectivity is towards HCOOH relative to CO, as evidenced by the overpotential for HCOOH (0.44 eV) being less than that for CO (1.07 eV) formation.

**CuSn<sub>3</sub>.** For gas-phase CuSn<sub>3</sub>, the electrochemical CO<sub>2</sub>-to-CO conversion is highly unfavourable because of the strong CO\* adsorption ( $\Delta G_{\text{CO}^*} = 2.2$  eV). In comparison, the highest free

energy of the reaction step for the HCOOH pathway is  $\Delta G_{\text{HCOOH(g)}} = 0.9$  eV. The CuSn<sub>3</sub> cluster is, therefore, selective towards the formation of HCOOH. In the Cu<sub>3</sub>Sn/ $\gamma$ -Al<sub>2</sub>O<sub>3</sub> system, the \*OCHO formation ( $\Delta G_{\text{OCHO}^*} = -0.5$  eV) is more favourable than COOH\* formation ( $\Delta G_{\text{COOH}^*} = -0.1$  eV). The subsequent steps from \*COOH to \*CO ( $\Delta G_{\text{CO}^*} = 1.4$  eV) and from \*OCHO to HCOOH ( $\Delta G_{\text{HCOOH}} = 1.2$  eV) are unfavourable. The HCOOH reaction pathway is lower compared to CO in this system. For the CuSn<sub>3</sub>/graphene system, the \*OCHO intermediate ( $\Delta G_{\text{OCHO}^*} = -0.7$  eV) is more favourable than \*COOH ( $\Delta G_{\text{COOH}^*} = -0.3$  eV). The subsequent steps for both initial intermediates have a positive Gibbs free energy ( $\Delta G_{\text{CO}^*} = 0.8$  eV and  $\Delta G_{\text{HCOOH(g)}} = 1.0$  eV). Moreover, the limiting potential for the electrochemical pathways shows CO (0.83 V) to be slightly lower than HCOOH (0.95 V).

The correlation of the Bader charge of Cu of supported clusters with the overpotential for the eCO<sub>2</sub>R reactions to HCOOH and CO is reported in Fig. 8. For both reaction pathways, the greater the negative charge on Cu, the higher the overpotential. The only exceptions are Cu<sub>4</sub> and Cu<sub>3</sub>Sn on  $\gamma$ -Al<sub>2</sub>O<sub>3</sub>. Since the site for CO<sub>2</sub> adsorption on the clusters is always the Cu atom (see Fig. S4, ESI<sup>†</sup>), a higher charge transferred to the Cu atoms will lead to stronger binding of the intermediates. However, there is a difference in the charge distribution on the catalyst depending on the support. For the



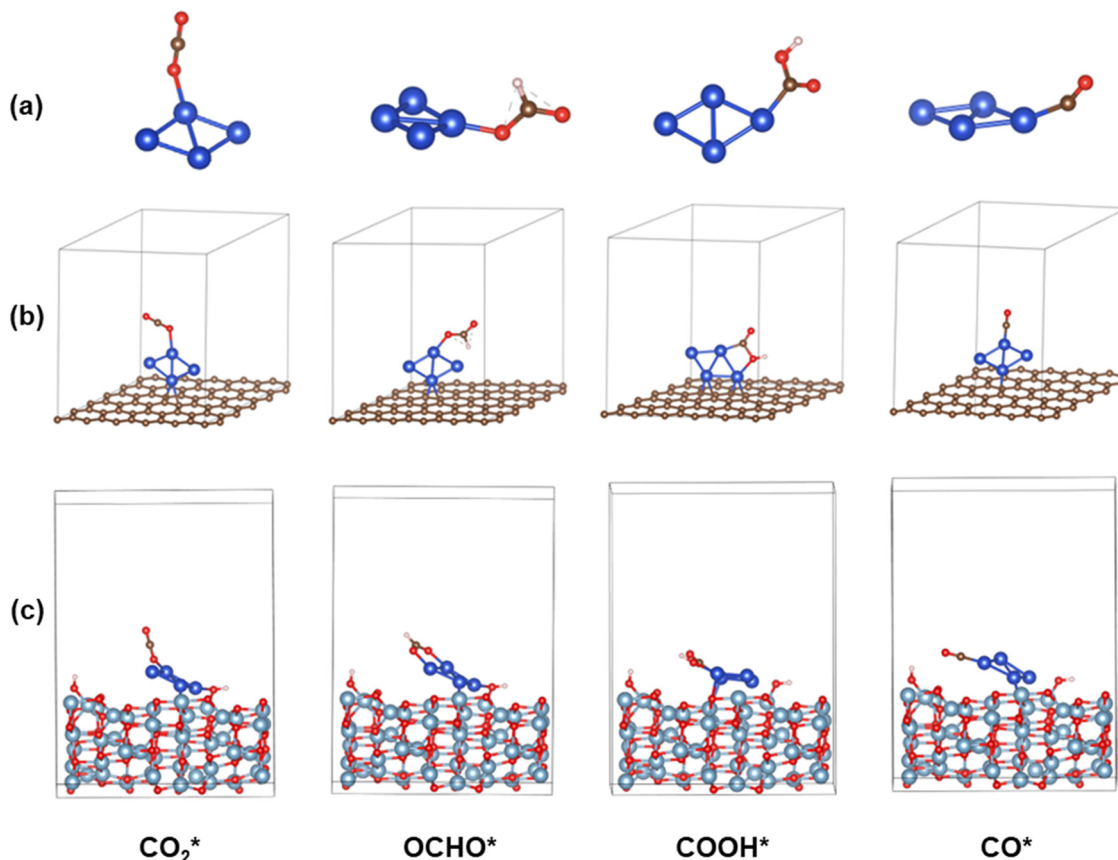


Fig. 7 Optimized structures of the  $\text{CO}_2^*$ ,  $\text{OCHO}^*$ ,  $\text{COOH}^*$ , and  $\text{CO}^*$  intermediates on (a)  $\text{Cu}_4$ , (b)  $\text{Cu}_4/\text{graphene}$ , and (c)  $\text{Cu}_4/\gamma\text{-Al}_2\text{O}_3$  (110). Blue, grey, brown, red and white balls represent Cu, Al, C, O and H atoms, respectively.

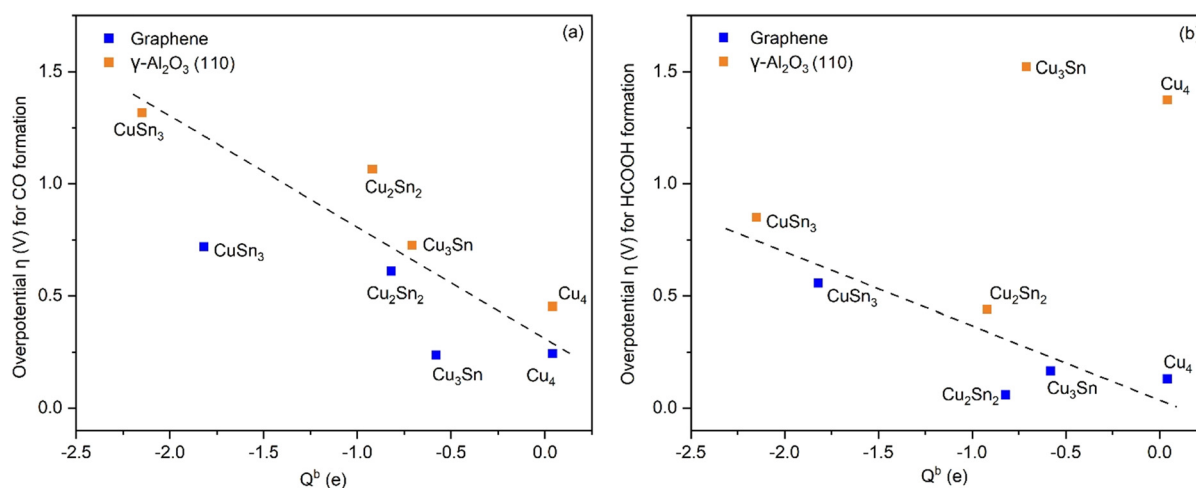


Fig. 8 Overpotential for CO and HCOOH formation as a function of the Bader charge,  $Q^b$ , of Cu in the Cu–Sn clusters supported on graphene (blue) and  $\gamma\text{-Al}_2\text{O}_3$  (orange). The dashed black lines in both figures serve as a guide to the eye.

$\text{Cu-Sn}$  clusters on  $\gamma\text{-Al}_2\text{O}_3$ , the Bader charge of Cu is higher compared to the case when the support is graphene. This behavior correlates with a higher overpotential for the reactions on  $\text{Cu-Sn}/\gamma\text{-Al}_2\text{O}_3$  (*vide infra*). Overall, the cluster composition and support influence the reaction energetics and hence the final product selectivity. This shows the importance of tuning

the properties of the active sites to tune the binding of the intermediates to control the selective formation of a specific product.

**3.4.2 Hydrogen evolution reduction.** Since  $\text{eCO}_2\text{R}$  occurs in aqueous solutions, there is always a competition between  $\text{CO}_2\text{R}$  and HER ( $\text{H}^+ + \text{e}^- \rightarrow 1/2 \text{H}_2$ ). The faradaic efficiency of HER is



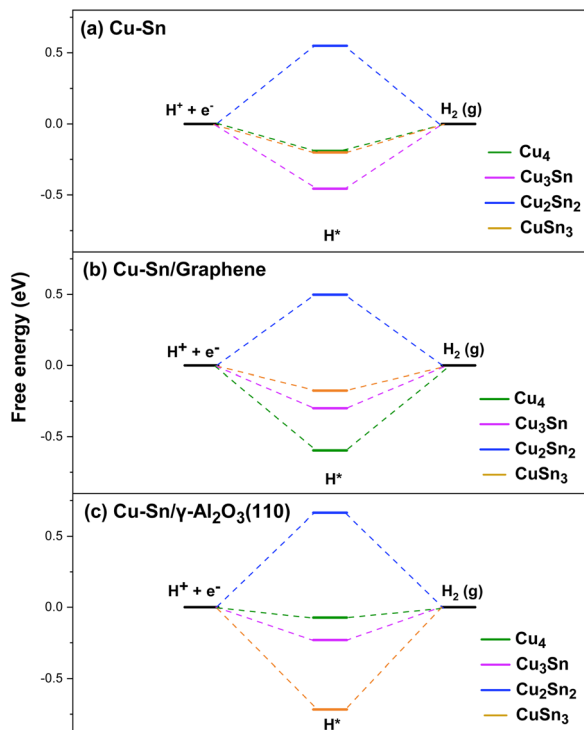


Fig. 9 Gibbs free energy diagram for the HER pathways to HCOO and CO on the (a) Cu<sub>4</sub>, (b) Cu<sub>3</sub>Sn, (c) Cu<sub>2</sub>Sn<sub>2</sub>, and (d) CuSn<sub>3</sub> clusters. Reduction pathways on isolated Cu<sub>4–n</sub>Sn<sub>n</sub> ( $n = 1–3$ ) clusters (light purple) and clusters supported on graphene (blue) and on the partially hydroxylated (110) surface of  $\gamma$ -Al<sub>2</sub>O<sub>3</sub> (orange).

usually higher than that of CO<sub>2</sub>R due to its much lower overpotential on most metallic catalysts. It was proposed that Sn could weaken the binding strength of H suppressing the HER.<sup>14</sup> Therefore, we have also computed the free energy of H adsorption ( $\Delta G_{H^*}$ ) on the Cu and Cu–Sn clusters to determine the role of Sn incorporation in the selectivity towards the CO<sub>2</sub>R rather than the HER. In Fig. 9(a), for the isolated Cu and Cu–Sn clusters the H adsorption is favorable on Cu<sub>4</sub> ( $\Delta G_{H^*} = -0.19$  eV), Cu<sub>3</sub>Sn ( $-0.45$  eV), and CuSn<sub>3</sub> ( $-0.21$  eV). In comparison, the value of  $\Delta G_{H^*}$  computed at the DFT-PBE level of theory for the copper (100) surface is  $-0.21$  eV.<sup>54</sup> On the other hand, Cu<sub>2</sub>Sn<sub>2</sub> has the highest Gibbs free energy of H adsorption (0.55 eV). The order from least to most favorable for the HER is Cu<sub>2</sub>Sn<sub>2</sub> > Cu<sub>4</sub> > CuSn<sub>3</sub> > Cu<sub>3</sub>Sn. For the clusters supported on graphene, Fig. 9(b), Cu<sub>2</sub>Sn<sub>2</sub> has, again, a positive free energy ( $\Delta G_{H^*} = 0.50$  eV), while the H adsorption is favorable on Cu<sub>4</sub> ( $\Delta G_{H^*} = -0.60$  eV), Cu<sub>3</sub>Sn ( $\Delta G_{H^*} = -0.30$  eV) and CuSn<sub>3</sub> ( $\Delta G_{H^*} = -0.18$  eV). The order from least to most favorable for the HER is Cu<sub>2</sub>Sn<sub>2</sub>/graphene > CuSn<sub>3</sub>/graphene > Cu<sub>3</sub>Sn/graphene > Cu<sub>4</sub>/graphene. Similarly, for the clusters supported on  $\gamma$ -Al<sub>2</sub>O<sub>3</sub>, Fig. 9(c), Cu<sub>2</sub>Sn<sub>2</sub> has the highest Gibbs free energy for H adsorption ( $\Delta G_{H^*} = 0.66$  eV). The H adsorption is favorable on Cu<sub>4</sub> ( $\Delta G_{H^*} = -0.07$  eV), Cu<sub>3</sub>Sn ( $\Delta G_{H^*} = -0.20$  eV), and CuSn<sub>3</sub> ( $\Delta G_{H^*} = -0.72$  eV). The order from least to most favorable for the HER is Cu<sub>2</sub>Sn<sub>2</sub>/ $\gamma$ -Al<sub>2</sub>O<sub>3</sub> > Cu<sub>4</sub>/ $\gamma$ -Al<sub>2</sub>O<sub>3</sub> > Cu<sub>3</sub>Sn/ $\gamma$ -Al<sub>2</sub>O<sub>3</sub> > CuSn<sub>3</sub>/ $\gamma$ -Al<sub>2</sub>O<sub>3</sub>. Overall, for both gas-phase and supported clusters, Cu<sub>2</sub>Sn<sub>2</sub> is highly unfavorable towards HER.

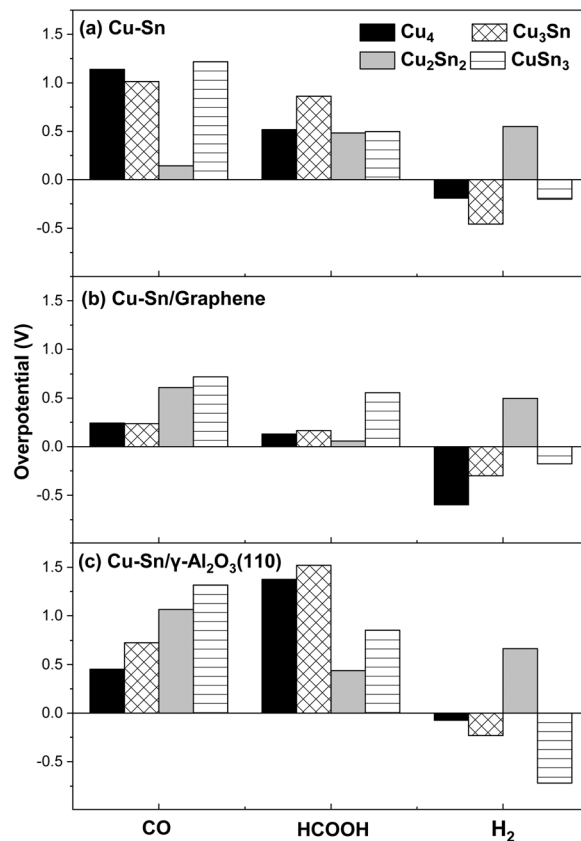


Fig. 10 Overpotential for the electrocatalytic formation of CO, HCOOH and H<sub>2</sub> on (a) isolated Cu<sub>n</sub>Sn<sub>2–n</sub>, (b) Cu<sub>n</sub>Sn<sub>2–n</sub>/graphene, and (c)  $\gamma$ -Al<sub>2</sub>O<sub>3</sub>.

**3.4.3 Selectivity.** The limiting potential ( $U_L$ ) and the overpotential ( $\eta$ ) are important factors for evaluating the catalytic activity of eCO<sub>2</sub>R electrocatalysts.<sup>55</sup> The limiting potential is given by the formula

$$U_L = -\Delta G_{\max}/ne \quad (6)$$

where  $\Delta G_{\max}$  is the free energy change of the rate-determining step at  $U = 0$  V,  $n$  is the number of electrons transferred, and  $e$  is the electron charge. The overpotential ( $\eta$ ) can then be obtained from the difference between the equilibrium potential ( $U_{eq}$ ) and the limiting potential ( $U_L$ ), which represents the minimum applied potential required to facilitate the formation of relevant intermediates:

$$\eta = U_{eq} - U_L \quad (7)$$

The magnitudes of the overpotential of the Cu–Sn catalysts for the eCO<sub>2</sub>R to CO, HCOOH and H<sub>2</sub> are summarized in Fig. 10(a–c). Poor catalytic performance towards a specific reaction is associated with a larger overpotential, and *vice versa*.

The eCO<sub>2</sub>R on the isolated Cu<sub>2</sub>Sn<sub>2</sub> cluster displays high selectivity towards CO since it has low overpotential (high catalytic activity) for CO formation (0.14 V) and high overpotential for H<sub>2</sub> (0.55 V) and HCOOH (0.48 V) formation (low catalytic activity). The Cu<sub>2</sub>Sn<sub>2</sub> catalyst could significantly enhance carbon monoxide selectivity because it is both less



selective to formic acid and suppresses HER. CO is the key intermediate in the mechanism of eCO<sub>2</sub>R on copper-based catalysts for the generation of C<sub>1</sub> and C<sub>2+</sub> value-added chemicals such as methane, methanol, ethanol, ethylene, and others.<sup>3</sup> On graphene, however, Cu<sub>2</sub>Sn<sub>2</sub> has the lowest overpotential for HCOOH (0.06 V) compared to the relatively high overpotential for CO (0.61 V) and H<sub>2</sub> (0.50 V) formation and, consequently, Cu<sub>2</sub>Sn<sub>2</sub> is selective towards formic acid. Of the  $\gamma$ -Al<sub>2</sub>O<sub>3</sub> supported clusters, Cu<sub>2</sub>Sn<sub>2</sub> has the lowest overpotential for HCOOH (0.44 V). However, it is more susceptible to the HER, as the overpotential for H<sub>2</sub> formation is only slightly higher (0.66 V). The other clusters show negative overpotentials for the HER and therefore are unlikely to be selective towards the eCO<sub>2</sub>R reaction. Overall, these results show the combined effects of the composition of the cluster and its supporting material on the selectivity towards CO, HCOOH or H<sub>2</sub>.

## 4. Conclusions

In this work, we conducted density functional theory calculations to characterize the properties of pristine Cu<sub>4-n</sub>Sn<sub>n</sub> ( $n = 0-4$ ) clusters and their ability to absorb, activate, and convert CO<sub>2</sub> to carbon monoxide (CO) and formic acid (HCOOH). We have divided the discussion of the calculations into four sections: (a) structure, stability, and electronic properties of Cu<sub>4-n</sub>Sn<sub>n</sub> clusters; (b) CO<sub>2</sub> binding and activation over the most stable systems; (c) kinetics of the gas phase CO<sub>2</sub> direct dissociation on Cu<sub>4-n</sub>Sn<sub>n</sub> clusters to generate CO; and (d) liquid-phase electrochemical CO<sub>2</sub> reduction reactions to CO and HCOOH on Cu<sub>4-n</sub>Sn<sub>n</sub> clusters and graphene and  $\gamma$ -Al<sub>2</sub>O<sub>3</sub> supported Cu-Sn clusters and their competition with the hydrogen evolution reaction. The energy descriptors, binding energy per atom and the second-order difference in energy, identify Cu<sub>2</sub>Sn<sub>2</sub> as the most stable cluster. The electronic energy descriptor HOMO-LUMO gap also suggests that the reactivity of the pure copper cluster, Cu<sub>4</sub>, is maintained for Cu<sub>2</sub>Sn<sub>2</sub> compared to the other Cu-Sn systems. Moreover, Cu<sub>2</sub>Sn<sub>2</sub> activates CO<sub>2</sub> as shown by pronounced bending of the linear O=C=O molecule. Calculations of the free energies for CO<sub>2</sub> reduction pathways to HCOOH and CO show that the isolated Cu<sub>2</sub>Sn<sub>2</sub> system has the highest potential as a stable and selective catalyst for the electrochemical CO<sub>2</sub> conversion to CO. But when supported on  $\gamma$ -Al<sub>2</sub>O<sub>3</sub> and graphene, the electrochemical CO<sub>2</sub> reduction on Cu<sub>2</sub>Sn<sub>2</sub> favors HCOOH formation, particularly over the Cu<sub>2</sub>Sn<sub>2</sub>/graphene catalyst. In addition, Cu<sub>2</sub>Sn<sub>2</sub> suppresses hydrogen evolution reaction. We can conclude that the isolated Cu<sub>2</sub>Sn<sub>2</sub> system has the highest potential as a stable and selective catalyst for the electrochemical CO<sub>2</sub> conversion to CO. When supported on graphene and  $\gamma$ -Al<sub>2</sub>O<sub>3</sub> (110) surfaces, Cu<sub>2</sub>Sn<sub>2</sub> can selectively generate HCOOH.

## Author contributions

Conceptualisation of work: AM, AGN and DDT; conduction of computations: AM and QZ; data analyses: AM and AGN, AR;

data dissemination & graphics: AM and DDT; writing of the manuscript: AM, AGN and DDT; project support: AR, DDT.

## Data availability

Raw data were generated at Queen Mary's Apocrita HPC facility. Derived data supporting the findings of this study are available from the corresponding author (DDT) on request.

## Conflicts of interest

The authors declare that the research was conducted in the absence of any commercial or financial relationships that could be construed as a potential conflict of interest.

## Acknowledgements

A.G.N acknowledges the Pakistan HEC-QMUL PhD Scholarships for funding. Q.Z. thanks the China Scholarship Council for financial support. D.D.T acknowledges the ACT programme (Accelerating CCS Technologies, Horizon2020 Project no. 294766), which funded the FUNMIN project. Financial contributions from the Department for Business, Energy & Industrial Strategy (BEIS) together with extra funding from NERC and EPSRC research councils, United Kingdom, ADEME (FR), and MINECO-AEI (ES) are acknowledged. We are grateful to the UK Materials and Molecular Modelling Hub for computational resources, which is partially funded by EPSRC (EP/T022213/1, EP/W032260/1 and EP/P020194/1). Via our membership of the UK's HEC Materials Chemistry Consortium, which is funded by EPSRC (EP/L000202), this work used the ARCHER UK National Supercomputing Service (<https://www.archer.ac.uk>). This research utilized Queen Mary's Apocrita HPC facility, supported by QMUL Research-IT, <https://doi.org/10.5281/zenodo.438045>.

## References

- 1 Y.-X. Duan, F.-L. Meng, K.-H. Liu, S.-S. Yi, S.-J. Li, J.-M. Yan and Q. Jiang, *Adv. Mater.*, 2018, **30**, 1706194.
- 2 J. Houghton, *Rep. Prog. Phys.*, 2005, **68**, 1343-1403.
- 3 S. Nitopi, E. Bertheussen, S. B. Scott, X. Liu, A. K. Engstfeld, S. Horch, B. Seger, I. E. L. Stephens, K. Chan, C. Hahn, J. K. Nørskov, T. F. Jaramillo and I. Chorkendorff, *Chem. Rev.*, 2019, **119**, 7610-7672.
- 4 R. Kortlever, J. Shen, K. J. P. Schouten, F. Calle-Vallejo and M. T. M. Koper, *J. Phys. Chem. Lett.*, 2015, **6**, 4073-4082.
- 5 X. Chen, J. Chen, N. M. Alghoraiibi, D. A. Henckel, R. Zhang, U. O. Nwabara, K. E. Madsen, P. J. A. Kenis, S. C. Zimmerman and A. A. Gewirth, *Nat. Catal.*, 2021, **4**, 20-27.
- 6 Q. Lu and F. Jiao, *Nano Energy*, 2016, **29**, 439-456.
- 7 B. Yang, C. Liu, A. Halder, E. C. Tyo, A. B. F. Martinson, S. Seifert, P. Zapol, L. A. Curtiss and S. Vajda, *J. Phys. Chem. C*, 2017, **121**, 10406-10412.



- 8 C. Liu, B. Yang, E. Tyo, S. Seifert, J. DeBartolo, B. von Issendorff, P. Zapol, S. Vajda and L. A. Curtiss, *J. Am. Chem. Soc.*, 2015, **137**, 8676–8679.
- 9 P. S. Sai Prasad, J. W. Bae, K.-W. Jun and K.-W. Lee, *Catal. Surv. Asia*, 2008, **12**, 170–183.
- 10 G. M. Tomboc, S. Choi, T. Kwon, Y. J. Hwang and K. Lee, *Adv. Mater.*, 2020, **32**, 1908398.
- 11 C. Liu, T. R. Cundari and A. K. Wilson, *J. Phys. Chem. C*, 2012, **116**, 5681–5688.
- 12 M. Zhang, Z. Zhang, Z. Zhao, H. Huang, D. H. Anjum, D. Wang, J. He and K.-W. Huang, *ACS Catal.*, 2021, **11**, 11103–11108.
- 13 Q. Li, X. Rao, J. Sheng, J. Xu, J. Yi, Y. Liu and J. Zhang, *J. CO<sub>2</sub> Util.*, 2018, **27**, 48–59.
- 14 M. Morimoto, Y. Takatsuji, R. Yamasaki, H. Hashimoto, I. Nakata, T. Sakakura and T. Haruyama, *Electrocatalysis*, 2018, **9**, 323–332.
- 15 H. Shin, K. U. Hansen and F. Jiao, *Nat. Sustain.*, 2021, **4**, 911–919.
- 16 H. Tao, Y. Li, X. Cai, H. Zhou, Y. Li, W. Lin, S. Huang, K. Ding, W. Chen and Y. Zhang, *J. Phys. Chem. C*, 2019, **123**, 24118–24132.
- 17 J. A. Rodriguez, J. Evans, L. Feria, A. B. Vidal, P. Liu, K. Nakamura and F. Illas, *J. Catal.*, 2013, **307**, 162–169.
- 18 A. Halder, L. A. Curtiss, A. Fortunelli and S. Vajda, *J. Chem. Phys.*, 2018, **148**, 110901.
- 19 L. E. Gálvez-González, J. O. Juárez-Sánchez, R. Pacheco-Contreras, I. L. Garzón, L. O. Paz-Borbón and A. Posada-Amarillas, *Phys. Chem. Chem. Phys.*, 2018, **20**, 17071–17080.
- 20 A. Alvarez-Garcia, E. Flórez, A. Moreno and C. Jimenez-Orozco, *Mol. Catal.*, 2020, **484**, 110733.
- 21 Megha, K. Mondal, T. K. Ghanty and A. Banerjee, *J. Phys. Chem. A*, 2021, **125**, 2558–2572.
- 22 S. Yin, T. Swift and Q. Ge, *Catal. Today*, 2011, **165**, 10–18.
- 23 C. Liu, H. He, P. Zapol and L. A. Curtiss, *Phys. Chem. Chem. Phys.*, 2014, **16**, 26584–26599.
- 24 F. Huang, Y. Deng, Y. Chen, X. Cai, M. Peng, Z. Jia, J. Xie, D. Xiao, X. Wen, N. Wang, Z. Jiang, H. Liu and D. Ma, *Nat. Commun.*, 2019, **10**, 4431.
- 25 L. Jin, B. Liu, P. Wang, H. Yao, L. A. Achola, P. Kerns, A. Lopes, Y. Yang, J. Ho, A. Moewes, Y. Pei and J. He, *Nanoscale*, 2018, **10**, 14678–14686.
- 26 J.-C. Liu, H. Xiao, X.-K. Zhao, N.-N. Zhang, Y. Liu, D.-H. Xing, X. Yu, H.-S. Hu and J. Li, *CCS Chem.*, 2022, **5**, 152–163.
- 27 D. Yang, S. Zuo, H. Yang, Y. Zhou, Q. Lu and X. Wang, *Adv. Mater.*, 2022, **34**, 2107293.
- 28 N. Sakamoto, Y. F. Nishimura, T. Nonaka, M. Ohashi, N. Ishida, K. Kitazumi, Y. Kato, K. Sekizawa, T. Morikawa and T. Arai, *ACS Catal.*, 2020, **10**, 10412–10419.
- 29 D. Du, H. Zhu, Y. Guo, X. Hong, Q. Zhang, B. Suo, W. Zou and Y. Li, *J. Phys. Chem. C*, 2022, **126**, 11611–11618.
- 30 G. Kresse and J. Furthmüller, *Comput. Mater. Sci.*, 1996, **6**, 15–50.
- 31 J. P. Perdew, K. Burke and M. Ernzerhof, *Phys. Rev. Lett.*, 1996, **77**, 3865–3868.
- 32 S. Grimme, J. Antony, S. Ehrlich and H. Krieg, *J. Chem. Phys.*, 2010, **132**, 154104.
- 33 G. Kresse and D. Joubert, *Phys. Rev. B: Condens. Matter Mater. Phys.*, 1999, **59**, 1758–1775.
- 34 G. Henkelman, B. P. Uberuaga and H. Jónsson, *J. Chem. Phys.*, 2000, **113**, 9901–9904.
- 35 A. J. Göttle and M. T. M. Koper, *Chem. Sci.*, 2017, **8**, 458–465.
- 36 J. Rossmeisl, Z. W. Qu, H. Zhu, G. J. Kroes and J. K. Nørskov, *J. Electroanal. Chem.*, 2007, **607**, 83–89.
- 37 K. Mathew, R. Sundararaman, K. Letchworth-Weaver, T. A. Arias and R. G. Hennig, *J. Chem. Phys.*, 2014, **140**, 84106.
- 38 Q. Zhang and A. Asthagiri, *Catal. Today*, 2019, **323**, 35–43.
- 39 H. A. Hansen, J. B. Varley, A. A. Peterson and J. K. Nørskov, *J. Phys. Chem. Lett.*, 2013, **4**, 388–392.
- 40 C. J. Pickard and R. J. Needs, *J. Phys.: Condens. Matter*, 2011, **23**, 53201.
- 41 V. V. Albert, S. A. Ivanov, S. Tretiak and S. V. Kilina, *J. Phys. Chem. C*, 2011, **115**, 15793–15800.
- 42 L. Tan, C. J. Pickard, K. Yu, A. Sapelkin, A. J. Misquitta and M. T. Dove, *J. Phys. Chem. C*, 2019, **123**, 29370–29378.
- 43 J. Gu, J. Wang and J. Leszczynski, *ACS Omega*, 2018, **3**, 1881–1888.
- 44 G. Paglia, C. E. Buckley, A. L. Rohl, R. D. Hart, K. Winter, A. J. Studer, B. A. Hunter and J. V. Hanna, *Chem. Mater.*, 2004, **16**, 220–236.
- 45 M. Yamamoto, Q. Zhao, S. Goto, Y. Gu, T. Toriyama, T. Yamamoto, H. Nishihara, A. Aziz, R. Crespo-Otero, D. D. Tommaso, M. Tamura, K. Tomishige, T. Kyotani and K. Yamazaki, *Chem. Sci.*, 2022, **13**, 3140–3146.
- 46 J. Gross, *J. Chem. Phys.*, 2009, **131**, 204705.
- 47 K. Jug, B. Zimmermann, P. Calaminici and A. M. Köster, *J. Chem. Phys.*, 2002, **116**, 4497–4507.
- 48 W. Tang, E. Sanville and G. Henkelman, *J. Phys.: Condens. Matter*, 2009, **21**, 084204.
- 49 G. Henkelman, A. Arnaldsson and H. Jónsson, *Comput. Mater. Sci.*, 2006, **36**, 354–360.
- 50 E. Sanville, S. D. Kenny, R. Smith and G. Henkelman, *J. Comput. Chem.*, 2007, **28**, 899–908.
- 51 S.-G. Wang, X.-Y. Liao, D.-B. Cao, C.-F. Huo, Y.-W. Li, J. Wang and H. Jiao, *J. Phys. Chem. C*, 2007, **111**, 16934–16940.
- 52 M. Xing, L. Guo and Z. Hao, *Dalton Trans.*, 2019, **48**, 1504–1515.
- 53 J. Niu, J. Ran, Z. Ou, X. Du, R. Wang, W. Qi and P. Zhang, *J. CO<sub>2</sub> Util.*, 2016, **16**, 431–441.
- 54 A. G. Nabi, A. ur-Rehman, A. Hussain and D. D. Tommaso, *Mol. Catal.*, 2022, **527**, 112406.
- 55 J.-H. Liu, L.-M. Yang and E. Ganz, *J. Mater. Chem. A*, 2019, **7**, 11944–11952.

